Inertial destabilization of highly viscous microfluidic stratifications

Xiaoyi Hu and Thomas Cubaud*
Department of Mechanical Engineering, Stony Brook University, Stony Brook, New York 11794, USA
(Received 25 April 2016; published 12 August 2016)

The hydrodynamic stability of stratifications made between miscible fluids having large differences in viscosity is experimentally investigated in square microchannels. Parallel fluid layers with a fast central stream and a slow sheath flow are produced by focusing a low-viscosity fluid into a high-viscosity fluid in a straight microchannel. Three regimes are identified and include diffusive, stable, and unstable flow patterns. In the unstable regime, coupled interfacial waves are seen to significantly disrupt strata when the Reynolds number associated with the low-viscosity stream is above 90. Several functional relationships are developed for the stratification width, propagating celerity, wavelength, amplitude, and frequency of interfacial waves over a range of viscosities and flow rates. We demonstrate, in particular, the wave phase locking for small central streams and show the production of high-viscosity fluid ligaments at the wave crests. In this case, a minute amount of high-viscosity fluid is entrained and blended into the low-viscosity fluid stream, thereby providing an original in-line mixing method for continuously adding a viscosifier to a thin fluid in microchannels.

DOI: 10.1103/PhysRevFluids.1.044101

I. INTRODUCTION

Stratified flows are common in natural environments and constitute a broad class of flows that exhibit a variety of wave motions [1]. When two fluids of different densities are superposed, the interface may be subject to Rayleigh-Taylor instabilities when the heavier fluid is on the top of the lighter fluid and Kelvin-Helmholtz instabilities when two fluids are in relative parallel motion [2], such as during the formation of ocean waves by wind and in billow clouds [3]. When fluids are stratified in viscosity, a wide range of shear flow instabilities can arise depending on layer configurations, velocities, temperature, as well as bulk and interfacial fluid properties for both miscible and immiscible fluid systems [4–7]. The stability of viscous stratifications and core-annular flows has been theoretically investigated for diverse confined parallel flow systems during the last decades [8–12]. While many numerical simulations were conducted for various flow configurations using either miscible [13] or immiscible fluids [14–16], relatively few experimental studies [17–20] have addressed the hydrodynamic stability of viscous-stratified flows using small scale experimental apparatuses.

Microfluidic platforms provide an idealized experimental environment to investigate novel flow configurations with high-viscosity fluids in the absence of significant gravitational effects [21–23]. In addition to Saffman-Taylor [24–27] and Rayleigh-Plateau [28–33] instabilities, multiphase flows in microgeometries encompass a wide range of fluid phenomena and are of great importance for a range of applications, such as oil and gas recovery [34], flow processing of viscous biomaterials [35], material synthesis [36,37], and drug discovery [38,39]. Among various microflow configurations, fluid stratifications are one of the simplest and permit the formation of longitudinal and transverse diffusion gradients, the destabilization of which can be used to enhance fluid mixing at the small scale [40–42]. To this end, multiple active and passive methods have been deployed to perturb parallel microfluidic layers, including electrokinetics, piezoelectric elements, oscillatory flows, wall modifications and specially designed two-dimensional (2D) or three-dimensional (3D)

*Author to whom correspondence should be addressed: thomas.cubaud@stonybrook.edu

 ©2016 American Physical Society

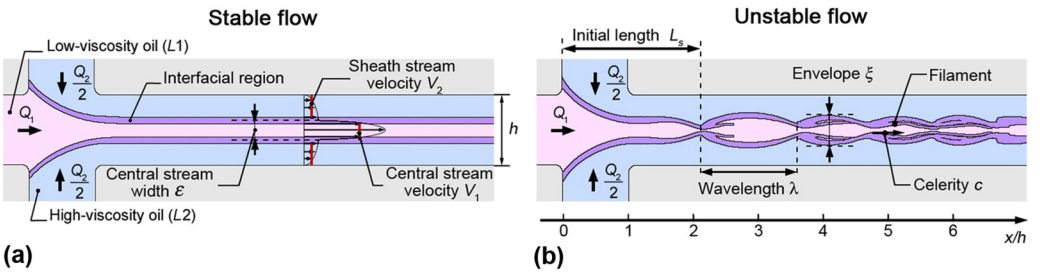

FIG. 1. Schematics of highly viscous microfluidic stratifications produced with hydrodynamic focusing showing (a) stable and (b) unstable flow configurations with notations.

channels [43–47]. When fluids have a large difference in viscosity, however, continuously blending low- and high-viscosity fluids is rather complex due to the evolution of the local viscosity as fluids mix along the fluidic system, and a better understanding of the behavior of viscosity-stratified flows in microchannels is needed.

In this article, we experimentally interrogate the stability of viscous stratifications made between miscible fluids in compact microchannels. In particular, we systematically investigate the three-layer fluid configuration that consists of a central stream made of a low-viscosity fluid in a sheath of a high-viscosity fluid that forms layers translating near the solid walls of a square microchannel. Liquids are injected into the microchannel with a symmetric hydrodynamic focusing section using a wide range of flow rates and fluid viscosities. We uncover multiple flow regimes and carefully examine the appearance and dynamics of traveling interfacial waves through the evolution of their wavelength, amplitude, frequency, and celerity above a critical Reynolds number. The simplicity of the flow configuration is chosen to clearly characterize the role of fluid properties and flow parameters on microscale flow destabilization processes. Indeed, highly symmetric hydrodynamic focusing sections can be used for the production of dissolving bubbles [48], droplets [49], and viscous threads [50]. Instead of investigating the influence of specific flow geometries for a particular application, we devote our efforts to delineate the regions in the parameter space where fluid phenomena can be generated using a single universal device. We thereby adopt somewhat of a "software" method, which maintains microchannel geometric and manufacturing simplicity, rather than methods that involve "hardware" modifications of microfluidic platforms to induce fluid mixing. Here, we specifically demonstrate that phase-locked traveling waves at each interface effectively produce recirculation cells in the low-viscosity central stream that can be used to enhance mixing of viscous ligaments detached from wave crests, which paves a route for the development of microfluidic methods for continuously adding a viscosifier to a thin fluid.

II. EXPERIMENTAL METHODS

A. Experiment setup

A hard microfluidic chip made of glass and silicon is employed to minimize channel deformations and withstand the large injection pressure required to drive high-viscosity fluids in microgeometries. A silicon wafer having a thickness $h = 250\ \mu$m is etched through in the flow region of interest using the Bosch process and sealed between two borosilicate glass plates using anodic bonding [51]. The resulting microfluidic module consists of a hydrodynamic focusing section composed of two square microchannels of height h that intersect perpendicularly (Fig. 1). The less viscous fluid $L1$, having a dynamic viscosity η_1, is introduced into the central channel at a volumetric flow rate Q_1 and the more viscous fluid $L2$, having a viscosity η_2, is symmetrically injected into the two side channels at a total volumetric flow rate Q_2 using syringe pumps. The chip is mounted onto an inverted microscope equipped with a high-speed camera and illuminated using a high-intensity fiber light on the other side of the device to examine the dynamics of viscous layers over a range of flow

TABLE I. Properties of fluid pairs with dynamic viscosities η_1 and η_2, viscosity contrast $\chi^{-1} = \eta_2/\eta_1$, diffusion coefficient D, Schmidt number Sc, and symbols.

Fluid pair	η_1 (cP)	η_2 (cP)	χ^{-1}	D (m^2/s)	Sc	Symbol
A	0.49	4865	9929	2.6×10^{-10}	2.5×10^3	△
B	0.49	971	1982	4.5×10^{-10}	1.5×10^3	◁
C	0.49	485	990	5.6×10^{-10}	1.2×10^3	◇
D	0.82	485	591	3.4×10^{-10}	3.0×10^3	▷
E	0.49	194	396	7.7×10^{-10}	8.4×10^2	◯
F	1.28	485	379	2.2×10^{-10}	6.9×10^3	⊙
G	0.49	97	198	9.8×10^{-10}	6.6×10^2	□
H	2.69	485	180	1.0×10^{-10}	2.9×10^4	⊡
I	0.49	48	98	1.2×10^{-9}	5.2×10^2	▽

rates and viscosity ratios $\chi = \eta_1/\eta_2$. Depending on fluid properties and flow parameters, a variety of stable and unstable stratifications are observed in the main outlet square channel. Stratifications are labeled as stable when the width ε of the less viscous central stream remains uniform along the flow direction and unstable when propagating undulations of wavelength λ, amplitude A, and celerity c develop at the fluid interfaces at a distance L_s from the fluid junction. To study the spatial evolution of "viscous waves," we use a coordinate system that starts in the focusing section (Fig. 1).

B. Fluid pairs

The model fluid pairs used are conventional silicone oils of different viscosities (Table I). As these oils are fully miscible, the diffusion coefficient D associated with each fluid pair is estimated using the Stokes-Einstein relationship together with the fluid molecular weights provided by the manufacturer (Gelest) and published experimental data [21,52]. A systematic series of experiments is conducted varying Q_1 and Q_2 using nine different fluid pairs to examine the influence of the viscosity ratio χ between stratifications. Since χ is very small, we typically refer to fluid pairs based on their viscosity contrast $\chi^{-1} = \eta_2/\eta_1$, which approximately ranges between 10^2 and 10^4. To clarify the role of absolute viscosities in the development and evolution of waves at the interface of microfluidic viscous layers, we also examine the flow behavior associated with fluid pairs having similar viscosity contrasts but different absolute viscosities, such as fluid pairs E and F and fluid pairs G and H (Table I). The Schmidt number associated with the low-viscosity fluid $\mathrm{Sc} = \eta_1/(\rho_1 D)$, where ρ_1 is the density of $L1$, is relatively small so we expect to observe flow phenomena involving both mass and momentum diffusion processes [53]. In turn, variations of both flow parameters and fluid properties allow us to study the influence of two important dimensionless groups, including the central stream Reynolds number $\mathrm{Re}_1 = \rho_1 V_1 h/\eta_1$, where V_1 is the corresponding average stream velocity defined as $V_1 = Q_1/(\varepsilon h)$, and the Péclet number $\mathrm{Pe} = h(J_1 + J_2)/D$ based on the sum of the superficial velocities of each fluid defined as $J_i = Q_i/h^2$, where the index $i = 1$ or 2 refers to fluids $L1$ or $L2$.

III. FLOW MAPS

We first examine the influence of the injection flow rates Q_1 and Q_2 on microfluidic stratifications and generate phase diagrams based on external control parameters for each fluid pair [Fig. 2(a)]. Three typical flow regimes are observed and include diffusive, stable, and unstable flow patterns [Fig. 2(b)]. Although mass diffusion phenomena are present in our miscible fluid flow system, significant convective mass transport can produce a straight interface in the field of view near the fluid junction at moderate velocities. We label this situation as the stable regime. By contrast,

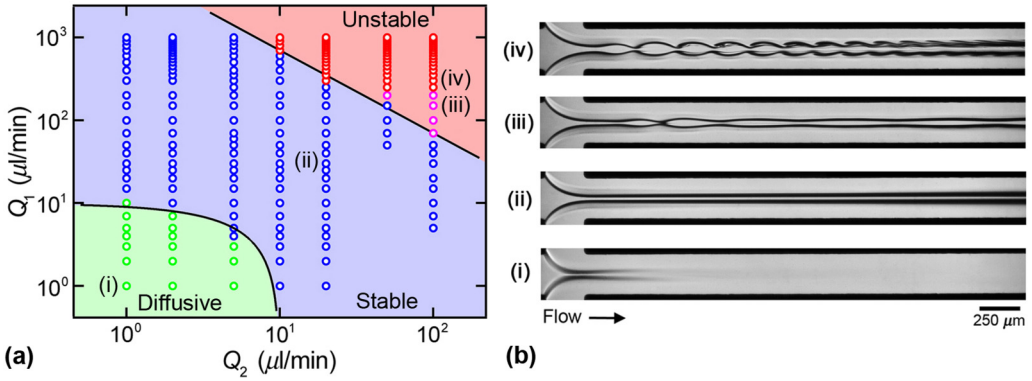

FIG. 2. (a) Dimensional flow map of diffusive, stable, and unstable regimes, flow rate Q_1 vs flow rate Q_2, fluid pair E. Transition curves: diffusive-stable, $Q_1 + Q_2 = Q_S = 10$ μl/ min, and stable-unstable, $(Q_1 Q_2)^{1/2} = Q_U = 84$ μl/ min. (b) Corresponding micrographs of typical flow regimes, flow rates in μl/ min: (i) diffusion regime, $Q_1 = 1$ and $Q_2 = 1$; (ii) stable regime, $Q_1 = 50$ and $Q_2 = 20$; (iii) transitional regime, $Q_1 = 200$ and $Q_2 = 100$; (iv) unstable regime, $Q_1 = 400$ and $Q_2 = 100$.

the diffusive regime is found for low velocities and is characterized with fading fluid interfaces, which can no longer be identified at the end of the channel. For all fluid pairs investigated with a variation of diffusion coefficients D over a decade (Table I), we find that the diffusion regime occurs for a relatively low Péclet number $\mathrm{Pe} = h(J_1 + J_2)/D < 860$, i.e., below a specific total superficial velocity $J_\mathrm{T} = J_1 + J_2$ for each fluid pair, which corresponds to the sum of the flow rates $Q_1 + Q_2 = Q_\mathrm{S}$, where Q_S is a constant, as can be seen on the flow map [Fig. 2(a)]. While both diffusive and stable regimes are steady state and flow structures appear static in the experimental field of view, the unstable flow regime is characterized by the formation of traveling waves at the fluid interfaces at large injection velocities. Two distinct wave patterns are discerned in this case. One is found near the transition with the stable regime and the wave structure is characterized with a wavelength λ that increases along the flow direction (x direction). The other one occurs for larger velocity and constitutes the typical unstable regime where the wavelength λ decreases along the flow direction. An estimation of the transition from the stable to wavy unstable flow regime on each flow map is characterized with a scaling of the form $Q_1 \sim Q_2^{-1}$ [Fig. 2(a)]. Therefore, the transition is approximated by the geometric mean of the flow rate $(Q_1 Q_2)^{1/2} \sim Q_\mathrm{U}$, where Q_U is a constant that depends on fluid properties. Overall, since the transition appears above a critical velocity, we label this regime as inertial instability. Instability waves are usually symmetric at two interfaces, which produce a series of instability cells for the central stream.

IV. DIFFUSIVE REGIME

The diffusive regime offers insights into the architecture and evolution of stratifications made of miscible and high-viscosity fluids in confined microgeometries. The spatial development of the lateral intensity profile along the flow direction is an indicator of the influence of diffusive phenomena and allows for differentiating the diffusive and stable regimes shown in Fig. 2. As molecular diffusion gradually blurs the boundary region between fluids, the relatively long residence times associated with low velocities promote a certain degree of fluid mixing. A comparative study of the evolution of the lateral grayscale intensity profile is conducted between the diffusive and stable cases [Fig. 3(a)]. In the diffusive regime ($\mathrm{Pe} = 260$), the deep valleys in the grayscale profile of the interfacial regions are quickly lifted and flattened along the flow direction [Fig. 3(a)]. At the end of the observation channel, the grayscale is nearly constant in the transverse flow direction, which suggests fluid mixing as the boundary between $L1$ and $L2$ is no longer observable. By contrast, for stable strata ($\mathrm{Pe} = 19\,000$), the grayscale profile remains relatively unchanged throughout the observation region

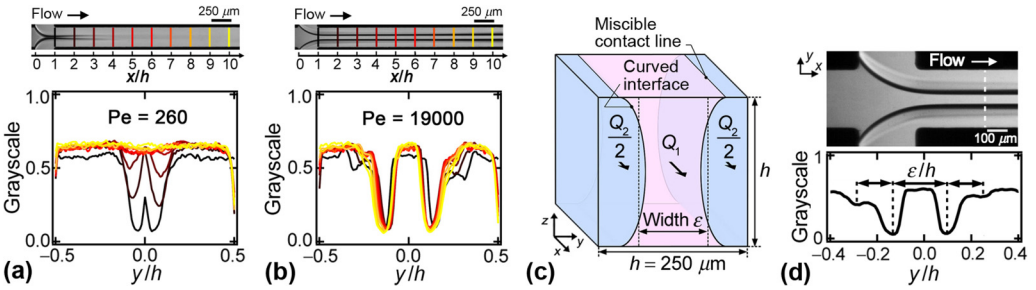

FIG. 3. Evolution of transverse grayscale intensity profile (flow rates in μl/ min): (a) diffusive regime, $Q_1 = 1$, $Q_2 = 2$, and Pe $= 260$; (b) stable regime, $Q_1 = 200$, $Q_2 = 20$, and Pe $= 19\,000$ (fluid pair E). (c) Schematics of flow configuration with curved interfaces due to self-lubrication effect. (d) Measurement of stable central stream width ε from global minima in intensity profile at $x/h \sim 2$.

and the intensity profile displays sharp variations, which suggests that diffusion has a rather limited effect on the interfacial region and diffusive mixing is negligible when the central stream flow rate Q_1 and side stream flow rates Q_2 are moderate.

Figure 3(c) shows a schematic representation of the deduced interfacial arrangement per cross section. Analysis of the intensity profile normal to the flow direction also reveals complex dynamic structures with the presence of local and global minima [Fig. 3(d)]. As the index of refraction of silicone oils depends on molecular weight, the occurrence of peaks and valleys in the intensity profile of the parallel flow of viscosity-differing oils indicates the presence of curved interfaces between fluids. Although confocal microscopy studies have shown that the interfacial region between fluids of different viscosities adopts a circular shape in plane microchannels [54,55], the strong confinement associated with the square channel and the presence of two interfaces in our system decreases the interfacial curvature compared to a circular arc. This phenomenon accounts for the so-called "self-lubrication" phenomenon [56] where fluids tend to rearrange so that the dissipation is minimized and the low-viscosity fluids tend to migrate to the regions of high shear stress, i.e., near walls, while high-viscosity sheath flow $L2$ favors regions of low shear. Here, the darker region indicates an interfacial configuration near parallel to incident light and is used to estimate the average position of the curved interface. Specifically, the central flow width ε is defined as the distance between two global minimums in the grayscale analysis of light intensity in the cross stratification direction [Fig. 3(d)]. At the transition between diffusive and stable regimes for Pe ~ 860, the flow morphology includes a broadening of the central width ε along the flow direction. For larger Pe, the width ε typically reaches a constant value after a relatively short distance $x/h \sim 2$ from the junction with negligible broadening further downstream, which indicates a stable regime.

V. STABLE REGIME

The stable stratification regime is obtained when the central stream width ε remains uniform in the experimental field of view, which corresponds to $x/h \leqslant 10$. For a given fluid pair having a fixed viscosity ratio χ, we find that the central flow width ε in a square channel is a function of the flow rate ratio $\varphi = Q_1/Q_2$. For large φ, the central stream extends to most of the square channel, leaving slender high-viscosity fluid stratifications near the sidewalls, while for small φ, a narrow low-viscosity central stream is observed. In the case of miscible fluid stratifications in plane microchannels [21], a simple expression can be analytically deduced for predicting the central flow width ε assuming flat fluid interfaces and continuity of shear stresses at the fluid boundaries according to $\varepsilon/h = [1 + (\varphi\chi)^{-1}]^{-1}$. In the case of square channel geometry, however, the influence of the sidewalls is non-negligible and a significant deviation is observed between data and the previous relationship. To formulate an accurate expression for the central stream width ε over a

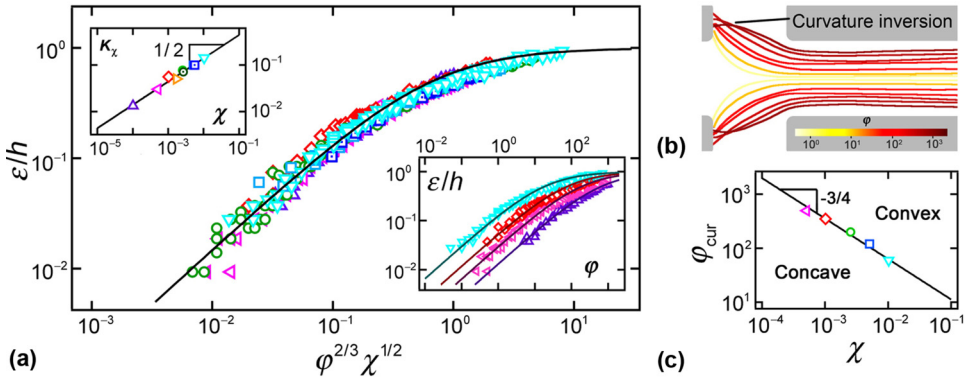

FIG. 4. (a) Stable central stream width ε/h as a function of $\varphi^{2/3}\chi^{1/2}$. Solid curve: $\varepsilon/h = [1 + (1.5\chi^{1/2}\varphi^{2/3})^{-1}]^{-1}$. Bottom inset: ε/h vs φ for fluid pairs A, B, C, and I. Data points are fitted with $\varepsilon/h = [1 + (K_\chi\varphi^{2/3})^{-1}]^{-1}$. Top inset: Coefficient K_χ as a function of χ. Solid line: $K_\chi = 1.5\chi^{1/2}$. (b) Composite image of interface locations at various φ for fluid pair B. (c) Critical flow rate ratio φ_{cur} for concave/convex central stream transition as a function of χ. Solid line: $\varphi_{\text{cur}} = 2\chi^{-3/4}$.

wide range of φ and χ, the stream width is systematically measured from micrographs using the lateral intensity profile of stratifications for all fluid pairs. To analyze data, we first focus on the influence of the flow rate ratio φ for a given viscosity ratio χ [Fig. 4(a), bottom inset]. Data show the expected monotonic increase of ε with φ and are well fitted with a functional relationship of the form $\varepsilon/h = [1 + (K_\chi\varphi^k)^{-1}]^{-1}$, where the coefficient K_χ represents the lateral shift of data points on the graph for various fluid pairs due to the viscosity ratio χ and the exponent $k = 2/3$ represents the steepness of the curve due to geometrical confinement. To quantify the effect of the viscosity ratio, we plot K_χ as a function of χ and deduce the scaling $K_\chi \sim a\chi^{1/2}$, where the constant $a \approx 1.5$ [Fig. 4(a), top inset]. Overall, the parameter $\varphi^{2/3}\chi^{1/2}$ allows for collapsing data points for all fluid pairs onto a single curve defined as

$$\frac{\varepsilon}{h} \approx \frac{1}{1 + 0.67\varphi^{-2/3}\chi^{-1/2}} \tag{1}$$

for $\varepsilon/h > 10^{-2}$. Normalized widths smaller than 1% are difficult to measure due to interfacial curvature and optical instrumental limitation, such as spatial resolution and depth of focus.

Another aspect of stable strata morphology is rooted in the relationship between the interfacial curvature in the y direction and φ as fluids are injected into the main channel [Fig. 4(b)]. In the focusing section, the central stream is found to adopt a convex shape with respect to the central stream when $Q_1 \gg Q_2$, and a concave form below a threshold value φ_{cur}. Over the range of viscosity contrasts investigated, we find that the critical flow rate ratio follows a scaling law such as $\varphi_{\text{cur}} \sim \chi^{-3/4}$ [Fig. 4(b)]. This relationship is interpreted as delineating the regime where viscous stresses associated with the central stream dominate flow behavior above φ_{cur} and the regime where sheath viscous stresses dictate flow morphology below φ_{cur}. For $\varphi > \varphi_{\text{cur}}$, data also suggest that viscous stratifications made of $L2$ are essentially confined to the sidewalls while the less viscous fluid $L1$ occupies most of the top and bottom walls of the square microchannel.

The central stream width ε is useful for estimating the average stream velocities according to $V_1 = Q_1/(\varepsilon h)$ for the central flow and $V_2 = Q_2/[(h - \varepsilon)h]$ for the sheath flow using mass conservation. According to Eq. (1), the stream velocity ratio can be expressed as $V_1/V_2 = (2/3)\varphi^{1/3}\chi^{-1/2}$. This relationship shows that very large velocity ratios are reached between the central and side streams for flow rate ratios larger than unity and for large viscosity contrasts. Such a large average velocity difference between streams is prone to shear-induced hydrodynamic instabilities.

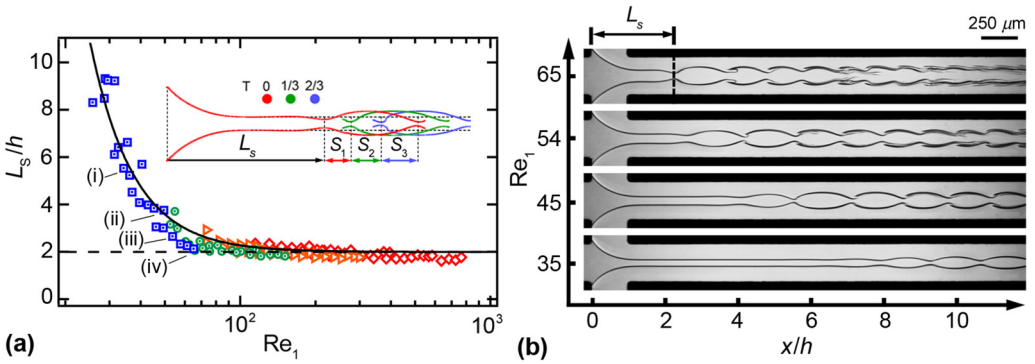

FIG. 5. (a) Instability developing length L_s/h as a function of Re_1 for fluid pairs having $\eta_2 = 485$ cP. Solid line: $L_s/h = 2 + (60/\mathrm{Re}_1)^{2.5}$; dashed line: $L_s/h = 2$. Inset: Superimposition of waves over a cycle. (b) Micrographs showing the evolution of L_s for Re_1 corresponding to data points (i)–(iv) in (a), fluid pair H.

VI. UNSTABLE REGIMES

Beyond the stable regime, various waves are observed at stratification interfaces above a set of critical injection velocities for each fluid pair. Information gained about the stable central stream width ε and velocity $V_1 = Q_1/(h\varepsilon)$ allows us to define the Reynolds number Re_1 according to $\mathrm{Re}_1 = \rho_1 V_1 h/\eta_1 = \rho_1 Q_1/(\varepsilon\eta_1)$. In the section, we show that strata are significantly destabilized when $\mathrm{Re}_1 \geqslant 90$. The Reynolds number associated with the sidewall stratification $\mathrm{Re}_2 = \rho_2 V_2 h/\eta_2 = \rho_2 Q_2/[(h-\varepsilon)\eta_2]$ is typically orders of magnitude lower than Re_1 due to the very large difference in viscosity $\eta_2 \gg \eta_1$ and velocity $V_1 \gg V_2$. As a result, it becomes possible to obtain a base flow where inertia plays a significant role in the fast central stream flow behavior while the slow and highly viscous stratifications are strongly laminar and display creeping flow characteristics. The presence of two inflection points in the average velocity profile is also an indication that this configuration is inherently unstable to disturbances [57]. Here, we take advantage of the versatility of microfluidic devices for fast screening of flow parameters and we conduct a detailed analysis of wave patterns and evolution. We first examine the onset of the appearance of waves at the fluid interface and delineate a stability phase diagram based on stream width ε and Reynolds number Re_1. We then provide detailed measurements of the morphology and dynamics of microfluidic propagating waves at viscous interfaces. Finally, we study the flow evolution further downstream with the formation of ligaments and filaments from wave crests.

A. Flow transitions

In the unstable regime, the wavelength λ of disturbances typically decreases along the flow direction. Near the transition with the stable case, however, a regime where the wavelength increases along the flow direction is observed. For moderate values of the central stream width ε, instability patterns are seen to develop at a certain distance L_s from the junction. For a given fluid pair, the instability developing length L_s can be adjusted with the central stream Reynolds number Re_1 (Fig. 5). To better understand the onset of the unstable regime, we quantitatively define L_s when the central stream ε reaches its first spatial minimum from the junction, which corresponds to the first wave crest [Fig. 5(a) inset]. For Re_1 ranging between 10 and 90, the length L_s/h sharply decreases with the Reynolds number Re_1 before reaching an asymptotic value $L_s/h \approx 2$. For fluid pairs having $\eta_2 = 485$ cP, data are fitted with a functional relationship of the form $L_s/h = 2 + (60/\mathrm{Re}_1)^{2.5}$ [Fig. 5(a)]. Examples of flow patterns during the transition are displayed in Fig. 5(b), where the wavelength λ spatially increases for low $\mathrm{Re}_1 \approx 35$ and decreases for larger $\mathrm{Re}_1 \approx 65$. In the classification of flow patterns, the developing length L_s/h is used as a reference for defining unstable regimes for cases where instability patterns are observed for moderate values of the central stream widths ε_0/h.

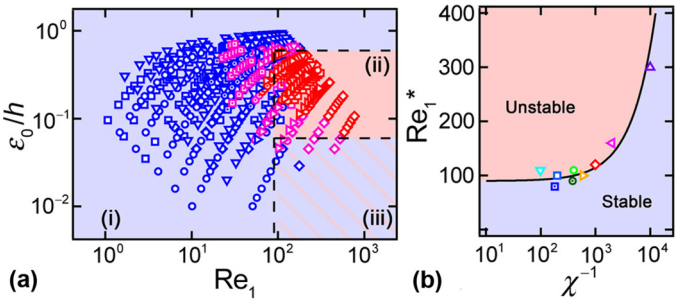

FIG. 6. (a) Stability phase diagram ε_0/h as a function of Re_1 with (i) stable regime, (ii) unstable region for $\mathrm{Re}_1 \geqslant 90$ and $0.6 \geqslant \varepsilon_0/h \geqslant 0.06$, and (iii) unexplored region, All fluid pairs except A and B. (b) Critical central Reynolds number Re_1^* as a function of χ^{-1} for all fluid pairs. Solid line: $\mathrm{Re}_1^* = 90 + \chi^{-1}/40$.

This occurs specifically for cases with a normalized instability developing length L_s/h near 2, while other cases are considered as transitional.

In addition to the central stream Reynolds number Re_1, another important parameter for the classification of viscous stratification flow regimes consists in the average stream width ε_0. Since, in the stable regime, the width ε depends only on the flow rate ratio $\varphi = Q_1/Q_2$ and is independent of absolute values of Q_1 and Q_2 for a given fluid pair, we use the correlation developed in Eq. (1) to estimate the reference width ε_0 for all flow configurations. This method allows for the generation of a dimensionless phase diagram in the parameter space (ε_0/h, Re_1) where stable and unstable flow regions are well defined [Fig. 6(a), (i) and (ii)]. In particular, a critical Reynolds number $\mathrm{Re}_1^* \approx 90$ for the transition between stable and unstable regimes is identified for low and moderate contrasts of viscosity $\chi^{-1} \leqslant 10^3$ [Fig. 6(a)]. Over the range of parameters investigated, the inertial instability appears in a square channel for a certain range of central stream widths ε_0/h bounded between 0.6 and 0.06. In practice, the formation of stratifications with very thin central streams $\varepsilon_0/h \ll 1$ at large Re_1 requires high-viscosity fluid flow rates Q_2 on the order of milliliters per minute, and this region remains unexplored on the diagram [Fig. 6(a), (iii)]. The upper bound for ε_0/h is found for thin strata in the high-shear regions near the walls. The critical Re_1^* is plotted as a function of the viscosity contrast χ^{-1} and fitted with $\mathrm{Re}_1^* = 90 + \chi^{-1}/40$ [Fig. 7(b)]. Data suggest that Re_1^* asymptotically increases as $\mathrm{Re}_1^* \sim \chi^{-1}$ for large viscosity contrasts $\chi^{-1} > 10^3$. This phenomenon illustrates the presence of a threshold for the resistance of a viscous fluid layer to inertial disturbances of an outer fluid in parallel flows corresponding to a viscosity contrast $\chi^{-1} \sim 10^3$. For very large viscosity contrasts, the fluid layer viscosity η_2 plays an important role in stabilizing stratifications

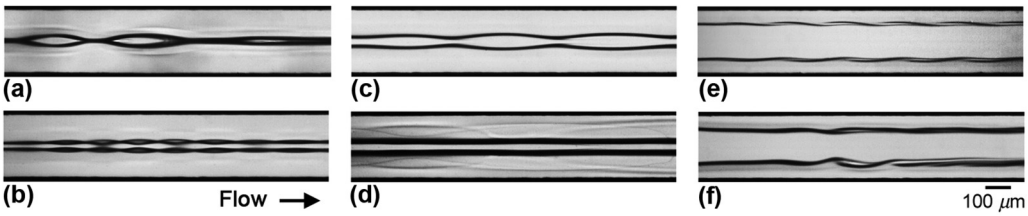

FIG. 7. Examples of transitional instability flow patterns. (a) Pinching instability ($\varepsilon_0/h = 0.05$, $\mathrm{Re}_1 = 225$, fluid pair C). (b) Braiding instability pattern ($\varepsilon_0/h = 0.07$, $\mathrm{Re}_1 = 146$, fluid pair E). (c) Increasing wavelength pattern ($\mathrm{Re}_1 = 96$, $\varepsilon_0/h = 0.11$, fluid pair E). (d) Lubrication/contact line instability pattern ($\varepsilon_0/h = 0.42$, $\mathrm{Re}_1 = 146$, fluid pair A). (e) Out-of-phase instability pattern ($\varepsilon_0/h = 0.71$, $\mathrm{Re}_1 = 32$, fluid pair H). (f) Nonsymmetric waves ($\varepsilon_0/h = 0.63$, $\mathrm{Re}_1 = 106$, fluid pair D).

against inertial instabilities of the thin fluid, which is characterized with a higher critical Reynolds number Re_1^*.

A variety of intriguing transitional microflow morphologies are uncovered near Re_1^* while systematically investigating flow behaviors for each fluid pair (Fig. 7). For instance, when the central flow width ε_0 is very small, two subtle transitional flow regimes are identified, such as "pinching" and "braiding." In the pinching regime, viscous interfaces appear to touch one another in the entry region and form an instability pattern corresponding to a few low-viscosity fluid cells whose wavelength quickly increases along the flow direction. Due to the small volume of fluid in each cell, the opening of instability cells along the flow direction does not significantly increase the central stream width and stratifications remain in apparent contact [Fig. 7(a)]. For some cases where strata appear to almost touch each other, a braiding instability pattern is documented when the deformation of each layer is not uniform in the z direction but rather alternated between the top and bottom walls. Wave deformations in each fluid layer appear in opposite phases before the healing of stratifications further downstream [Fig. 7(b)]. For moderate central stream width ε_0, two unstable interfacial motifs are observed that correspond to the typical transitional case with a positive wavelength gradient [Fig. 7(c)] and to the situation of a lubrication/contact line destabilization [Fig. 7(d)]. In the latter case, engulfment of the low-viscosity fluid near the top or bottom walls of the channel produces a modification of the lubricated area between low- and high-viscosity fluids and miscible contact lines show wavy movements. Finally, when the central stream flow width is relatively large, the waves at each interface lose their synchronization [Figs. 7(e) and 7(f)]. Given the relatively small amplitude of interfacial deformations observed in this case, we interpret this behavior as a result of the large distance between interfaces ε, which prevents strong hydrodynamic coupling between stratifications.

Overall, transitional instability patterns show the duality in the approach of the problem of unstable viscous sheath flows where patterns form complex cells from the point of view of the central steam [18,19] or interfacial waves from the point of view of the stratifications [16]. In the following, we examine the morphology and dynamics of the unstable regime to experimentally clarify the phenomenon of inertial deformations of highly viscous layers in microfluidics.

B. Inertial regimes

In this section, we conduct a detailed investigation of the influence of flow parameters and fluid properties on wave morphology, including envelope size ξ, amplitude A, and wavelength λ, as well as on dynamics, such as frequency f and celerity c. The formation and transport of slender flow structures from wave crests, including ligaments, is also discussed.

1. Morphology

a. Wavelength. We first examine the evolution of the perturbation wavelength λ along the flow direction x. Image processing routines are developed to track wave crest positions from high-speed experimental videos using the open source program IMAGEJ. For a given experimental micrograph, wave crests correspond to local minima of the central stream width ε. Spatiotemporal diagrams of the crest positions are constructed to extract the wavelength $\lambda(x)$ defined as the distance between two adjacent traces and x corresponds to the central position between two crests [Fig. 8(a), top]. The wavelength evolution $\lambda(x)$ for a given fluid pair and flow rates is then produced by superimposing wavelengths detected over several time periods T [Fig. 8(a), bottom]. In the unstable regime, data show a smooth and a regular spatial evolution with a significant increase of λ from the focusing section to about $x/h \approx 2$, where a maximum value $\lambda_{\max}$ is reached before a gradual decrease is observed further downstream.

The maximum wavelength $\lambda_{\max}$ provides a useful parameter to quantify the morphology of viscous stratification waves across a range of fluid properties. Figure 8(b) displays the normalized wavelength $\lambda_{\max}/h$ as a function of the low-viscosity fluid flow rate Q_1. Although the wavelength initially slightly increases and then minimally decreases with Q_1, the overall change of $\lambda_{\max}/h$ is

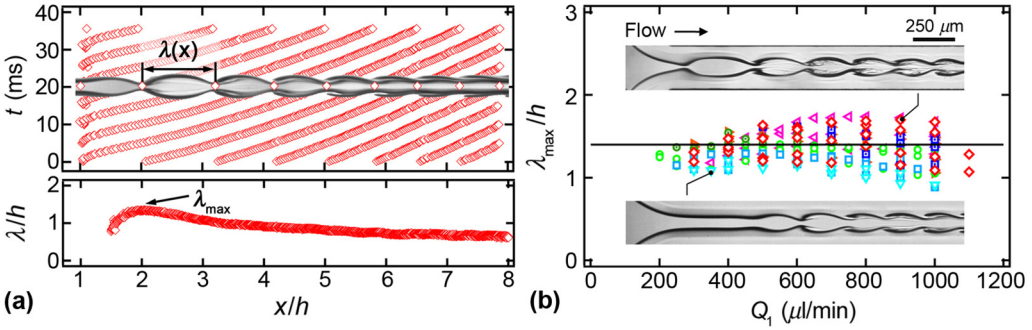

FIG. 8. (a) Measurement of instantaneous wavelength $\lambda(x)$ from spatiotemporal evolution of wave crests ($Q_1 = 400$ and $Q_2 = 50$ μl/ min, fluid pair C). (b) Normalized maximum wavelength λ_{max}/h as a function of Q_1. Solid line: $\lambda_{max}/h = 1.4$. Top inset: $Q_1 = 900$ and $Q_2 = 100$ μl/ min, fluid pair C. Bottom inset: $Q_1 = 300$ and $Q_2 = 100$ μl/ min, fluid pair I.

negligible for variations of viscosity contrasts and flow rates over decades. In particular, data show that the maximal wavelength can be approximated with a constant value $\lambda_{max}/h \approx 1.4$ throughout our experiments. The spatial evolution of the wave crests encompasses various processes, such as the formation of various slender viscous structures typically referred to as ligaments and flow self-healing mechanisms where the wave amplitude A decays along the flow and wave crests become effectively suppressed further downstream.

b. Cell envelope and wave amplitude. Another important shape parameter consists in the amplitude A of wave deformations of each interface. Given the complex developing appearance of waves, however, it is more accurate in practice to examine the envelope evolution of the central stream $\xi(x)$ instead of directly measuring relatively small wave amplitudes $A(x)$ at each interface. The envelope size is typically obtained by superimposing hundreds of experimental micrographs from a single high-speed movie into a composite image [Fig. 9(a) inset]. This method permits the detection of $\xi(x)$ by using image processing and data shows that, similar to the wavelength evolution, a maximum ξ_{max} is reached near the fluid focusing section where the first central stream cell appears [Fig. 9(a)]. In general, we focus our analysis of the envelope size on the upstream region of the microchannel where wave trains are well defined and negligibly influenced by diffusion or ligament-induced deformations. Thus, the quantity ξ_{max} is used as the characteristic value for the envelope size. Since

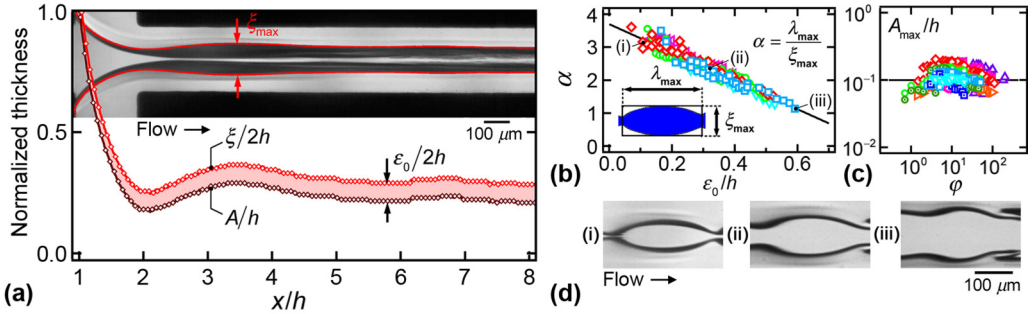

FIG. 9. (a) Spatial evolution of cell envelope ξ and wave amplitude A, $Q_1 = 600$ and $Q_2 = 50$ μl/ min, fluid pair C. (b) Cell aspect ratio α as a function of ε_0/h. Solid line: $\alpha = 3.7-4.3\varepsilon_0/h$ (fluid pairs A, B, C, E, G, and I). (c) Normalized wave amplitude A_{max}/h vs φ for all fluid pairs. Solid line: $A_{max}/h = 10^{-1}$. (d) Example of cell aspect ratio (i) $\alpha = 3.16$, $\varepsilon_0/h = 0.11$, fluid pair C, (ii) $\alpha = 2.2$, $\varepsilon_0/h = 0.33$, fluid pair G, and (iii) $\alpha = 1.14$, $\varepsilon_0/h = 0.59$, fluid pair G.

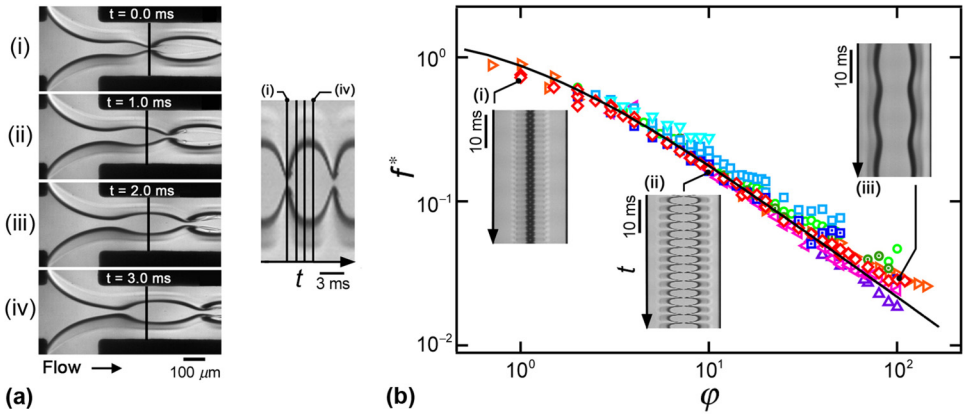

FIG. 10. (a) Measurement of wave emission period $T = f^{-1}$. Left: Time series of micrographs. Right: Corresponding spatiotemporal diagram ($Q_1 = 500$ and $Q_2 = 50\ \mu$l/ min, fluid pair C). (b) Normalized frequency $f^* = f/\gamma$ vs flow rate ratio φ of all fluid pairs. Solid line: $f^* = 1.75(1+\varphi^{0.95})^{-1}$. Insets: Spatiotemporal diagrams with similar resolutions, fluid pair C, flow rates in μl/ min: (i) $Q_1 = 200$ and $Q_2 = 200$, (ii) $Q_1 = 500$ and $Q_2 = 50$, and (iii) $Q_1 = 1000$ and $Q_2 = 10$.

λ_{max} and ξ_{max} usually appear at a similar position x, we define the cell aspect ratio $\alpha = \lambda_{max}/\xi_{max}$ to characterize the morphology of the first instability cell for the central stream. As the reference width ε_0 is varied, cell aspect ratios α for all fluid pairs collapse onto a single curve, which can be fitted using the function $\alpha = 3.7-4.3\varepsilon_0/h$ [Fig. 9(b)]. This result shows that as the central stream becomes wider, the cell aspect ratio tends to unity. The maximum envelope size ξ_{max} is also used to calculate the corresponding maximum amplitude $A_{max} = (\xi_{max} - \varepsilon_0)/2$ of waves at each fluid interface. The normalized wave amplitude remains relatively constant $A_{max}/h \approx 10^{-1}$ for a wide range of flow rate ratios φ. Together with the data for the wavelength, our work shows that the aspect ratio of waves remains more or less constant, $\lambda_{max}/A_{max} \approx 14$, regardless of fluid viscosities or flow rates of injection in the unstable regime.

2. *Dynamics*

a. Frequency. A fundamental aspect of interfacial waves is rooted in their period of emission T. Our microfluidic apparatus, along with its high-speed imaging capabilities, allows us to examine a range of wave frequencies $f = T^{-1}$. Using a typical camera acquisition rate of 5×10^3 frames per second, the time period T is measured from spatiotemporal diagrams made along a line drawn normal to the flow direction at $x/h \approx 2$ [Fig. 10(a)]. We find experimentally that waves are generated at very regular frequencies. To nondimensionalize our results, the frequency f is calculated from the measurements of the time period T and normalized with the average flow shear rate γ defined as $\gamma = 2J_T/h$, where J_T is the superficial velocity $J_T = (Q_1 + Q_2)/h^2$. Data points for the nondimensional frequency $f^* = f/\gamma$ fall onto a single curve when plotted as a function of flow rate ratio φ [Fig. 10(b)]. Over the range of parameters investigated, a simple relationship of the form

$$f^* = \frac{1.75}{1+\varphi^{0.95}} \tag{2}$$

allows a good correlation. It is remarkable that the frequency f does not depend on the viscosity ratio χ, despite the importance of this parameter on the central stream width ε and the rather large velocity ratio V_1/V_2 between stratifications. In addition, the experimentally measured exponent of 0.95 is close to unity, which suggests proportionality between the wave frequency and the homogeneous fraction $f^* \sim Q_2/(Q_1 + Q_2)$ of the high-viscosity fluid. As opposed to the situation of dispersed

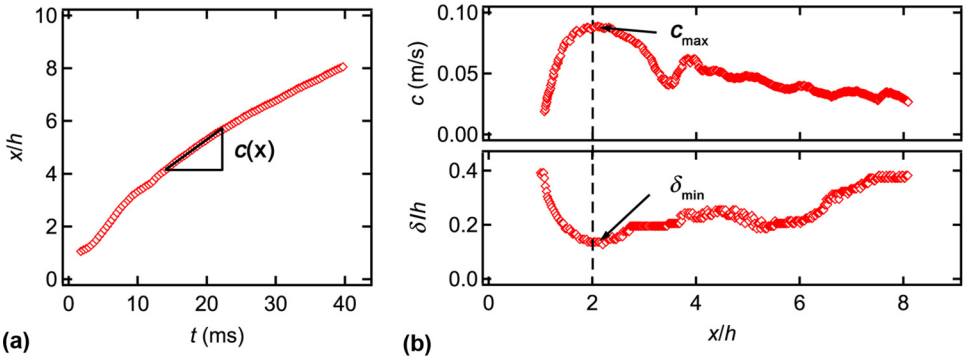

FIG. 11. (a) Example of evolution of wave crest position x as a function of time t ($Q_1 = 500$ and $Q_2 = 50$ μl/ min, fluid pair C). (b) Top: Corresponding celerity $c(x)$ where the maximum celerity $c_{\max}$ is found at around $x/h = 2$. Bottom: Evolution of crest separation distance normalized by channel height δ/h with a minimum at around $x/h = 2$.

flows, however, the concept of fluid fraction in the context of separated flows with large average slip between phases requires further investigation, and additional experimental and theoretical efforts are needed to better understand this phenomenon.

b. Celerity. One of the most important features of wave phenomena consists in the speed of propagation. To measure the instantaneous wave celerity c, the average position x of a crest as a function of time t is first extracted from spatiotemporal diagrams of the minimum central stream width [Fig. 11(a)]. Data for multiple wave crests are combined and averaged to calculate the wave velocity for a given flow condition through numerical differentiation of the crest position with respect to time t [Fig. 11(b), top]. In a fashion similar to the spatial evolution of the wavelength λ, we observe a maximum celerity $c_{\max}$ near the fluid junction at $x/h \approx 2$. The evolution of the distance δ between coupled crests is also measured along the flow direction x [Fig. 11(b), bottom]. As expected from mass conservation, the minimum distance $\delta_{\min}$ appears at a similar location to $c_{\max}$ since the maximum velocity is reached for the smallest throat size of the cell.

The maximum celerity $c_{\max}$ is a useful parameter to examine the effect of fluid properties and flow parameters on interfacial wave dynamics. For all fluid pairs, $c_{\max}$ is measured and plotted as a function of the flow rate ratio φ [Fig. 12(a)]. A striking feature of our experimental investigation

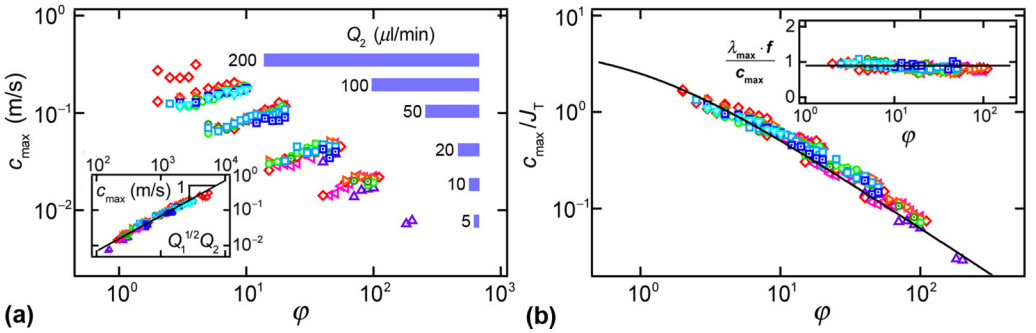

FIG. 12. Maximum wave celerity $c_{\max}$ as a function of flow rate ratio φ; data form distinct curves based on Q_2. Inset: Maximum celerity $c_{\max}$ vs scaling parameter $Q_1^{1/2}Q_2$. Solid line: $c_{\max} = K Q_1^{1/2} Q_2$, with $K = 10^{12}$ m$^{-7/2}$ s$^{1/2}$. (b) Normalized celerity $c_{\max}/J_T$ as a scaling function of φ. Solid line: $c_{\max}/J_T = 5(1 + \varphi^{0.95})^{-1}$. Inset: Independent measurements of f, $c_{\max}$, and $\lambda_{\max}$ yield consistent wave equation $f\lambda_{\max} \sim c_{\max}$. Solid line: $f\lambda_{\max}/c_{\max} = 0.9$.

is the grouping of data points on specific curves according to the sheath flow rate Q_2 regardless of the viscosity ratio χ of each fluid pair [Fig. 12(a)]. For a fixed sheath flow rate Q_2, the celerity $c_{\max}$ shows a weak increase with φ, which in this case is directly proportional to Q_1. We find it surprising that the side flow rate Q_2 has a stronger influence on the wave propagation celerity $c_{\max}$ compared to Q_1 despite its relatively small value, i.e., $Q_1 \gg Q_2$ for $\varphi \gg 1$. In the pursuit of a scaling relationship for the wave celerity $c_{\max}$ based on the flow rates of injection, we investigate the possibility to relate $c_{\max}$ to a quantity of the form $Q_1^a Q_2^b$, where the values of exponents a and b capture the relative influence of each stream on the wave celerity. The inset of Fig. 12(a) shows that such a scaling law appears very consistent with the experimental data for coefficients $a = 1/2$ and $b = 1$ as measurements of $c_{\max}$ for all fluid pairs fall onto a single curve defined by $c_{\max} = K Q_1^{1/2} Q_2$, where K is a dimensional coefficient equaling 10^{12} $\mathrm{m}^{-7/2}\,\mathrm{s}^{1/2}$. Although such a direct relationship is useful for evaluating the absolute value of $c_{\max}$, the rather obscure meaning of the units and value of K suggest that a more straightforward dimensionless approach might succeed in predicting $c_{\max}$.

Since both λ and c reach a maximum value around $x/h \approx 2$, the basic wave relationship $c_{\max} = \lambda_{\max} f$ used in conjunction with the fact that $\lambda_{\max}/h \approx 1.4$ indicates that $c_{\max}$ should essentially scale with f. To validate our assumption, independently measured frequency f, maximum wavelength $\lambda_{\max}$, and celerity $c_{\max}$ are related according to the ratio $\lambda_{\max} f/c_{\max}$, which remains close to unity for a range of two decades in φ for all fluid pairs [Fig. 12(b) inset]. Therefore, to express the maximal celerity $c_{\max}$ directly as a function of the input control parameters Q_1 and Q_2, we normalize the celerity with the total superficial velocity J_{T}, which is proportional to the average shear rate γ. This method allows for the collapse of all data points onto a single curve [Fig. 12(b)], defined according to

$$\frac{c_{\max}}{J_{\mathrm{T}}} = \frac{5}{1+\varphi^{0.95}}. \tag{3}$$

This dimensionless relationship for the maximum celerity [Eq. (3)] has the same type of dependency on the flow rate ratio $\varphi = Q_1/Q_2$ with an exponent of 0.95 as the equation for the dimensionless frequency f^* [Eq. (2)]. Based on these correlations, the maximal wavelength $\lambda_{\max}/h$ is expected to range around 1.27, which is very close to the measured average value of 1.4. Although the viscosity ratio χ does not influence the initial wave propagation speed c, the evolution of wave crests is strongly affected by fluid properties.

c. Ligaments. A stunning feature of interfacial wave phenomena is typically found during the breaking and rolling of wave crests. The very large difference in average stream velocities in our case produces the entrainment of highly viscous filamentous structures from the crests into the miscible, low-viscosity central stream. The miniature and slender structures of such ligaments make them particularly sensitive to diffusion phenomena as they evolve along the flow direction. This crest erosion phenomena between miscible fluids are mainly responsible for the self-healing process of stratification observed at moderate values of Q_1 [Fig. 13(a)]. For higher values of Q_1, a ligamentous structure persists and evolves along a complex array of slow moving cells formed by the phase-locked waves at each interface. Incidentally, cells of high aspect ratio α, which are found for low ε_0, provide a dynamic recirculation chamber in which filaments can form two nearly symmetric vortical structures from each crest, which overall promotes fluid mixing due to the large interfacial area of the ligaments [Fig. 13(b)]. Rotating vortices are also seen to elongate along the flow direction. This mechanism can be employed to blend a small amount of high-viscosity oil into a low-viscosity solvent. The quantity of viscous fluid entrained from the crest increases with the cell aspect ratio α as narrow central streams produce larger ligaments [Fig. 13(c)]. The tips of the ligaments are best identified for fluid pairs having low diffusion coefficients [Fig. 13(d)]. Arising from symmetric crests, the tips of the ligaments appear to slide along the main fluid interface as they elongate due to the large central stream speed near the channel axis, which is in contrast with the cases of immiscible fluids where droplets form at the ligament tip [58]. At the secondary wave crests downstream, ligaments further interact with the wave structure as they sequentially come together and drift apart and additional viscous fluid is carried away in the central stream. The formation of

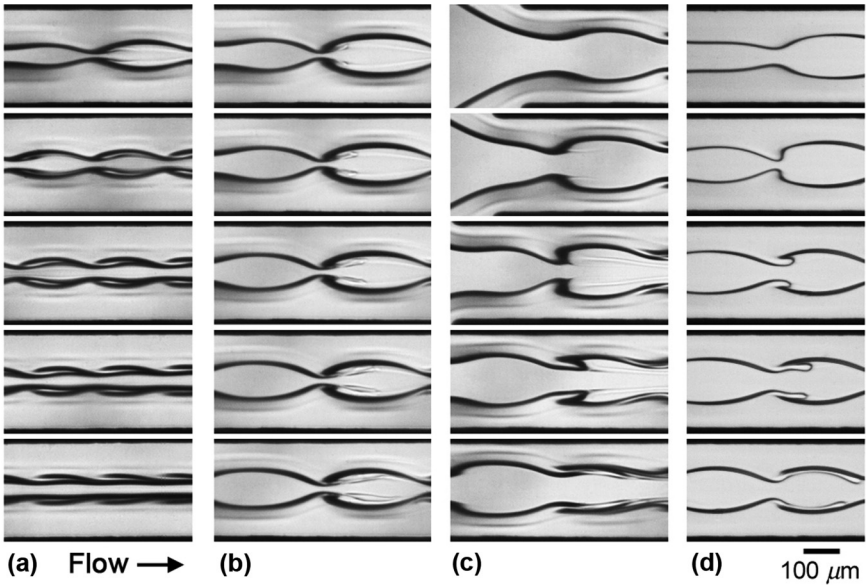

FIG. 13. Time series of micrographs showing ligament and vortex formation in the reference frame of a crest (from top to bottom, flow rates in μl/ min). (a) Self-healing flow ($Q_1 = 300, Q_2 = 50$, fluid pair $C, \Delta t =$ 8.8 ms). (b) Formation of vortex ($Q_1 = 1000, Q_2 = 50$, fluid pair C, $\Delta t = 0.2$ ms). (c) Formation of ligament ($Q_1 = 1000, Q_2 = 20$, fluid pair C, $\Delta t = 3$ ms). (d) Ligament formation series ($Q_1 = 1000, Q_2 = 100$, fluid pair H, $\Delta t = 1$ ms).

multiple ligaments traveling much faster than the wave train along the fluid interface produces a range of downstream flow patterns.

d. Downstream flow patterns. The spatial development of multiphase flow instabilities can lead to increasingly intricate flow morphologies. A few typical cases of complex downstream flow patterns are displayed in Fig. 14. Although the most common flow regime observed consists of a healed wave where layers of ligaments progressively blend [Fig. 14(a)], a distorted cell can lead to a change of phase locking between the viscous layers at each wall, which is accompanied with a change from a varicose type of deformation, i.e., symmetric cells, to an asymmetric variation, i.e., corkscrew wave [Fig. 14(b)]. Another example of flow evolution consists in the merging of two adjacent cells producing irregular wavelength variations [Fig. 14(c)]. Finally, quite irregular patterns are observed

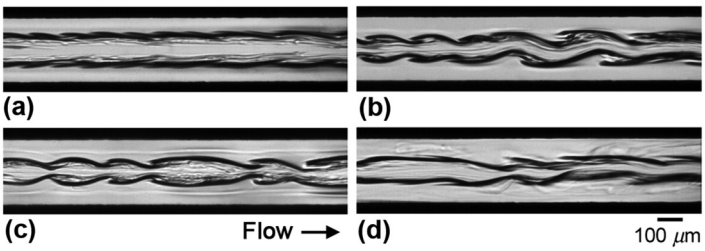

FIG. 14. Downstream flow patterns. Flow rates in μl/ min. (a) Healed waves ($Q_1 = 1000, Q_2 = 100$, fluid pair I). (b) Corkscrew waves ($Q_1 = 750, Q_2 = 100$, fluid pair E). (c) Merged cells ($Q_1 = 900, Q_2 = 100$, fluid pair C). (d) Disordered flow ($Q_1 = 1000, Q_2 = 50$, fluid pair B).

with a combination of corkscrew waves and long wavelength cells along with a strong deformation of contact lines [Fig. 14(d)]. Such flow patterns obtained for large viscosity contrasts and large flow rates between miscible fluids resemble those obtained between immiscible fluids at large capillary numbers.

VII. CONCLUSIONS

In this article, we discuss the formation and stability of viscous-stratified flows produced by symmetrically injecting a low-viscosity fluid into a flowing sheath of miscible and high-viscosity fluid using hydrodynamic focusing in square microchannels. Employing conventional silicone oils of various molecular weights as model fluid pairs, we systematically characterize the morphology and dynamics of viscous strata for a broad range of viscosities and flow rates. A typical flow map based on dimensional control parameters is first presented to delineate three major flow patterns, including a diffusive regime for small stream velocities, a stable regime for moderate flow rates, and an unstable regime, where interfacial waves significantly disrupt coflowing viscous layers, for high shear rates. Functional relationships for regime transitions are then developed based on detailed experimental measurements of the evolution of the intensity profile of fluid layers along the flow direction. A characteristic quantity consists of the central stream width ε that allows for estimating the average stream velocities, which are controlled with the flow rate ratio φ and the viscosity ratio χ. Information gained about the average stream width ε sets forth the development of a dimensionless phase diagram using the central stream Reynolds number Re_1. We present an overview of the unstable regime and introduce quantitative criteria, such as the instability developing length L_s, for the classification of a rich variety of transitional regimes. Above a critical $\mathrm{Re}_1^* \approx 90$ and for moderate viscosity ratios χ and stream widths ε, well-defined interfacial waves appear near the fluid junction. We investigate the influence of fluid properties on the morphology and dynamic features of interfacial waves and show that their maximal wavelength λ_{max} and amplitude A_{max} remain relatively constant. High-speed imaging allows us to independently acquire functional relationships for the frequency f and celerity c of waves traveling along the interface of fluids having a variety of large viscosity coefficients. We show, in particular, that phase-locked waves are independent of viscosity and vary according to both the relative and absolute flow rates of injection Q_1 and Q_2. This work clarifies the role of average, superficial, and interfacial velocities as well as fluid properties on the stability of confined viscous separated microflows.

The unstable regime offers useful features for implementing in-line mixing procedures between highly viscous fluids in microfluidic systems. The evolution of interfacial disturbances can indeed lead to the detachment of ligaments from wave crests and result in the blending of minute amounts of high-viscosity fluids with low-viscosity fluids. In this case, the configuration of a central stream made of a thin fluid layer encased into two coflowing layers of thick fluids allows for the formation of dynamic recirculating cells that enhance mixing. We study the rich phenomenology of ligament detachment and evolution along a complex miscible, multifluid system at the small scale. Although a full detailed experimental analysis covering all aspects of the flow regimes encountered in this work is beyond our efforts, we characterize a few basic hydrodynamic properties of stable and unstable viscous microstratifications that can serve as a basis for comprehensive theoretical and numerical studies. In addition to further elucidating passive mixing mechanisms between viscosity-differing fluids in microchannels, future studies are needed to better understand the subtle relationship between interfacial waves and fluid properties, including the effect of diffusion and interfacial tension, in confined microsystems. Linear and nonlinear hydrodynamic stability analyses would also shed light on the absolute or convective nature of inertial instabilities of viscosity stratified in compact microchannels. Overall, the relatively low critical Reynolds numbers required to initiate significant interfacial destabilization between high-viscosity fluids at the small scale suggest the possibility to readily reach a breadth of remarkable and relatively unexplored basic flow regimes with viscous fluids in high-pressure microfluidic platforms.

ACKNOWLEDGMENTS

We have appreciated discussions with Dr. Martin Sauzade and Professor Jie Yu. This material is based upon work supported by the National Science Foundation under Grant No. CBET-1150389.

[1] D. J. Tritton, *Physical Fluid Dynamics* (Oxford University Press, New York, 1988).
[2] S. Chandrasekhar, *Hydrodynamic and Hydromagnetic Stability* (Dover, New York, 1981).
[3] P. G. Drazin and W. H. Reid, *Hydrodynamic Stability* (Cambridge University Press, Cambridge, UK, 2004).
[4] K. Gage and W. Reid, The stability of thermally stratified plane Poiseuille flow, J. Fluid Mech. **33**, 21 (1968).
[5] C. E. Hickox, Instability due to viscosity and density stratification in axisymmetric pipe flow, Phys. Fluids **14**, 251 (1971).
[6] G. Ivey, K. Winters, and J. Koseff, Density stratification, turbulence, but how much mixing? Annu. Rev. Fluid Mech. **40**, 169 (2008).
[7] R. Govindarajan and K. C. Sahu, Instabilities in viscosity-stratified flow, Annu. Rev. Fluid Mech. **46**, 331 (2014).
[8] C.-S. Yih, Instability due to viscosity stratification, J. Fluid Mech. **27**, 337 (1967).
[9] C.-H. Li, Instability of three-layer viscous stratified flow, Phys. Fluids **12**, 2473 (1969).
[10] D. D. Joseph, M. Renardy, and Y. Renardy, Instability of the flow of two immiscible liquids with different viscosities in a pipe, J. Fluid Mech. **141**, 309 (1984).
[11] B. T. Ranganathan and R. Govindarajan, Stabilization and destabilization of channel flow by location of viscosity-stratified fluid layer, Phys. Fluids **13**, 1 (2001).
[12] B. Selvam, S. Merk, R. Govindarajan, and E. Meiburg, Stability of miscible core-annular flows with viscosity stratification, J. Fluid. Mech. **592**, 23 (2007).
[13] K. C. Sahu, H. Ding, P. Valluri, and O. K. Matar, Linear stability analysis and numerical simulation of miscible two-layer channel flow, Phys. Fluids **21**, 042104 (2009).
[14] P. Valluri, L. Ó. Náraigh, H. Ding, and P. Spelt, Linear and nonlinear spatio-temporal instability in laminar two-layer flows, J. Fluid Mech. **656**, 458 (2010).
[15] C. Kouris and J. Tsamopoulos, Dynamics of axisymmetric core-annular flow in a straight tube. I. The more viscous fluid in the core, bamboo waves, Phys. Fluids **13**, 841 (2001).
[16] L. Ó. Náraigh, P. Valluri, D. M. Scott, I. Bethune, and P. D. Spelt, Linear instability, nonlinear instability and ligament dynamics in three-dimensional laminar two-layer liquid–liquid flows, J. Fluid Mech. **750**, 464 (2014).
[17] P. Gondret and M. Rabaud, Shear instability of two-fluid parallel flow in a Hele-Shaw cell, Phys. Fluids **9**, 3267 (1997).
[18] Q. Cao, A. L. Ventresca, K. R. Sreenivas, and A. K. Prasad, Instability due to viscosity stratification downstream of a centerline injector, Can. J. Chem. Eng. **81**, 913 (2003).
[19] M. d'Olce, J. Martin, N. Rakotomalala, D. Salin, and L. Talon, Pearl and mushroom instability patterns in two miscible fluids' core annular flows, Phys. Fluids **20**, 024104 (2008).
[20] T. Al-Wahaibi and P. Angeli, Experimental study on interfacial waves in stratified horizontal oil–water flow, Int. J. Multiphase Flow **37**, 930 (2011).
[21] T. Cubaud and T. G. Mason, Formation of miscible fluid microstructures by hydrodynamic focusing in plane geometries, Phys. Rev. E **78**, 056308 (2008).
[22] T. Cubaud, B. M. Jose, and S. Darvishi, Folded micro-threads: Role of viscosity and interfacial tension, Phys. Fluids **23**, 042002 (2011).
[23] T. Cubaud, B. M. Jose, S. Darvishi, and R. Sun, Droplet breakup and viscosity-stratified flows in microchannels, Int. J. Multiphase Flow **39**, 29 (2012).
[24] G. M. Homsy, Viscous fingering in porous media, Annu. Rev. Fluid Mech. **19**, 271 (1987).
[25] E. Lajeunesse, J. Martin, N. Rakotomalala, D. Salin, and Y. C. Yortsos, Miscible displacement in a Hele-Shaw cell at high rates, J. Fluid Mech. **398**, 299 (1999).

[26] R. Balasubramaniam, N. Rashidnia, T. Maxworthy, and J. Kuang, Instability of miscible interfaces in a cylindrical tube, Phys. Fluids **17**, 052103 (2005).
[27] B. Jha, L. Cueto-Felgueroso, and R. Juanes, Fluid Mixing from Viscous Fingering, Phys. Rev. Lett. **106**, 194502 (2011).
[28] L. E. Johns and R. Narayanan, *Interfacial Instability* (Springer, New York, 2002).
[29] P. Guillot, A. Colin, A. S. Utada, and A. Ajdari, Stability of a Jet in Confined Pressure-Driven Biphasic Flows at Low Reynolds Numbers, Phys. Rev. Lett. **99**, 104502 (2007).
[30] A. S. Utada, A. Fernández-Nieves, H. A. Stone, and D. A. Weitz, Dripping to Jetting Transitions in Coflowing Liquid Streams, Phys. Rev. Lett. **99**, 094502 (2007).
[31] K. J. Humphry, A. Ajdari, A. Fernández-Nieves, H. A. Stone, and D. A. Weitz, Suppression of instabilities in multiphase flow by geometric confinement, Phys. Rev. E **79**, 056310 (2009).
[32] B. M. Jose and T. Cubaud, Formation and dynamics of partially wetting droplets in square microchannels, RSC Adv. **4**, 14962 (2014).
[33] S. L. Anna, Droplets and bubbles in microfluidic devices, Annu. Rev. Fluid Mech. **48**, 285 (2016).
[34] V. Berejnov, N. Djilali, and D. Sinton, Lab-on-chip methodologies for the study of transport in porous media: energy applications, Lab Chip **8**, 689 (2008).
[35] R. Gorkin *et al.*, Centrifugal microfluidics for biomedical applications, Lab Chip **10**, 1758 (2010).
[36] A. Günther and K. F. Jensen, Multiphase microfluidics: from flow characteristics to chemical and materials synthesis, Lab Chip **6**, 1487 (2006).
[37] S. Tottori and S. Takeuchi, Formation of liquid rope coils in a coaxial microfluidic device, RSC Adv. **5**, 33691 (2015).
[38] P. S. Dittrich and A. Manz, Lab-on-a-chip: microfluidics in drug discovery, Nat. Rev. Drug Discovery **5**, 210 (2006).
[39] L. Kang, B. G. Chung, R. Langer, and A. Khademhosseini, Microfluidics for drug discovery and development: From target selection to product lifecycle management, Drug Discovery Today **13**, 1 (2008).
[40] C. Y. Lee, C. L. Chang, Y. N. Wang, and L. M. Fu, Microfluidic mixing: A review, Int. J. Mol. Sci. **12**, 3263 (2011).
[41] V. Hessel, H. Löwe, and F. Schönfeld, Micromixers—a review on passive and active mixing principles, Chem. Eng. Sci. **60**, 2479 (2005).
[42] N.-T. Nguyen and Z. Wu, Micromixers—a review, J. Micromech. Microeng. **15**, R1 (2005).
[43] C.-C. Chang and R.-J. Yang, Electrokinetic mixing in microfluidic systems, Microfluid. Nanofluid. **3**, 501 (2007).
[44] A. Couairon and J.-M. Chomaz, Absolute and convective instabilities, front velocities and global modes in nonlinear systems, Physica D: Nonlinear Phenom. **108**, 236 (1997).
[45] A. D. Stroock, S. K. Dertinger, A. Ajdari, I. Mezić, H. A. Stone, and G. M. Whitesides, Chaotic mixer for microchannels, Science **295**, 647 (2002).
[46] H. Song, J. D. Tice, and R. F. Ismagilov, A microfluidic system for controlling reaction networks in time, Angew. Chem., Int. Ed. **42**, 768 (2003).
[47] M. S. Munson and P. Yager, Simple quantitative optical method for monitoring the extent of mixing applied to a novel microfluidic mixer, Anal. Chim. Acta **507**, 63 (2004).
[48] M. Sauzade and T. Cubaud, Initial microfluidic dissolution regime of CO_2 bubbles in viscous oils, Phys. Rev. E **88**, 051001(R) (2013).
[49] T. Cubaud and T. G. Mason, Capillary threads and viscous droplets in square microchannels, Phys. Fluids **20**, 053302 (2008).
[50] T. Cubaud and S. Notaro, Regimes of miscible fluid thread formation in microfluidic focusing sections, Phys. Fluids **26**, 122005 (2014).
[51] M. J. Madou, *Fundamentals of Macrofabrication and Nanotechnology*, Vol. II (CRC Press, Boca Raton, FL, 2012).
[52] N. Rashidnia, R. Balasubramaniam, J. Kuang, P. Petitjeans, and T. Maxworthy, Measurement of the diffusion coefficient of miscible fluids using both interferometry and Wiener's method, Int. J. Thermophys. **22**, 547 (2001).

[53] S. P. Vanka and C. M. Winkler, Numerical study of scalar mixing in curved channels at low Reynolds numbers, AIChE J. **50**, 2359 (2004).
[54] P. Guillot, P. Panizza, J. B. Salmon, M. Joanicot, A. Colin, C. H. Bruneau, and T. Colin, Viscosimeter on a microfluidic chip, Langmuir **22**, 6438 (2006).
[55] W. Engl, K. Ohata, P. Guillot, A. Colin, and P. Panizza, Selection of Two-Phase Flow Patterns at a Simple Junction in Microfluidic Devices, Phys. Rev. Lett. **96**, 134505 (2006).
[56] D. D. Joseph and Y. Y. Renardy, *Fundamentals of Two-Fluid Dynamics. Part II: Lubricated Transport, Drops and Miscible Liquids* (Springer, New York, 1993).
[57] P. Huerre and M. Rossi, in *Hydrodynamics and Nonlinear Instabilities*, edited by G. Godrèche and P. Manneville (Cambridge University Press, Cambridge, UK, 2005).
[58] T. Al-Wahaibi, M. Smith, and P. Angeli, Transition between stratified and non-stratified horizontal oil–water flows. Part II: Mechanism of drop formation, Chem. Eng. Sci. **62**, 2929 (2007).